

Low-Temperature Dehydrogenation of Vapor-Deposited Magnesium Borohydrides Imaged Using Identical Location Microscopy

Margaret Fitzgerald, Sarah Shulda, Nicholas A. Strange, Andreas Schneemann, Vitalie Stavila, Liwen F. Wan, Karl Gross, Thomas Gennett, Steven Christensen, Svitlana Pylypenko,* and Noemi Leick*

Cite This: *J. Phys. Chem. C* 2022, 126, 19024–19034

Read Online

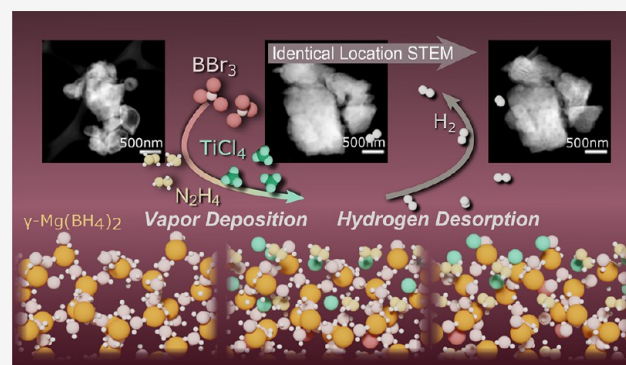
ACCESS |

Metrics & More

Article Recommendations

Supporting Information

ABSTRACT: Complex metal hydrides are promising hydrogen storage materials with their high volumetric and gravimetric capacities, but they are limited by high temperatures for hydrogen release and slow kinetics for hydrogen uptake. These limitations necessitate modifications to allow hydride materials to become more technologically viable. It has been shown that chemical additives can reduce the hydrogen desorption temperature and improve reaction rates of a hydride matrix. Currently, the most common method to integrate chemical additives is through ball milling. In contrast, this work investigates the vapor-phase delivery of chemical additives to the gamma phase of $\text{Mg}(\text{BH}_4)_2$, adapted from atomic layer deposition which uses sequential precursor exposures on a material surface to grow thin films. The modified $\text{Mg}(\text{BH}_4)_2$ materials demonstrated up to 7.6 wt % hydrogen release at temperatures as low as 100 °C. The materials in this work were characterized extensively using temperature-programmed desorption, the Sieverts method, and X-ray diffraction. Additionally, identical location scanning transmission electron microscopy was conducted to identify the chemical complexities of the modifications introduced from the vapor-phase delivery process and through the hydrogen desorption process. Findings from the microscopy study were combined with the aforementioned characterization techniques to illuminate the mechanism of decomposition and allow for a better understanding of the vapor-phase-modified materials. Overall, this work demonstrates how combining a diverse suite of characterization techniques, especially electron microscopy, enables the discovery and understanding of the sorption and chemical processes that take place in hydrogen storage materials and contribute to accelerate research in this field.



INTRODUCTION

Hydrogen is a key component of developing a carbon neutral economy that can connect multiple industrial and commercial sectors including energy production, storage, transportation, and manufacturing. For this reason, critical initiatives by the government and other stakeholders are necessary to further develop and integrate all relevant technologies.^{1–3} Hydrogen has a high energy density per mass, exhibits facile conversion to electricity, and is readily sourced. However, the energy density per volume for hydrogen poses a major barrier for storing and transporting hydrogen.⁴ The physical storage of hydrogen as a compressed gas or liquid requires high pressures or cryogenic temperatures which reduce the round-trip efficiency, require expensive tanks, and have dormancy issues (retention of stored H_2). Hydrogen stored in a solid, chemical state, as is the case for metal hydrides, often exceeds the volumetric density of liquid hydrogen (71 kg m^{-3}). For example, $\text{Mg}(\text{BH}_4)_2$ has theoretical densities of 82–117 kg m^{-3} for the most common structural

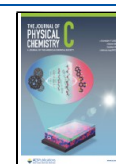
modifications. A primary challenge for application of metal hydrides as hydrogen storage media is the high temperatures needed to desorb hydrogen at adequate rates.

$\text{Mg}(\text{BH}_4)_2$ is a promising hydrogen storage material because it has one of the highest gravimetric and volumetric hydrogen density of all materials, and it has a lower dehydrogenation temperature (approximately 300 °C) compared to other metal borohydrides (Li and Na) which have desorption temperatures at or above 400 °C.^{5–7} In order for materials-based hydrogen storage to be a viable option for transportation applications, significant amounts of hydrogen must be released at temper-

Received: July 6, 2022

Revised: October 17, 2022

Published: November 4, 2022



atures $<200\text{ }^{\circ}\text{C}$.⁸ One method to improve the kinetics and temperature of desorption is to introduce low concentrations of chemical additives into the structure of the parent metal hydride.^{9,10} Most commonly, chemical additives are introduced by ball milling the metal hydride with main group and transition-metal compounds (halides, organics, oxides, and borides).^{11–13} However, ball milling can introduce unwanted contamination into metal hydrides (i.e., abrasion from the balls), alter the character of crystalline phases, and form thermodynamically irreversible states that reduce the hydrogen capacity.^{14–16} To reduce these effects seen from ball milling, alternative methods of chemical modification of $\text{Mg}(\text{BH}_4)_2$ are needed to improve hydrogen desorption parameters.

The structure of $\gamma\text{-Mg}(\text{BH}_4)_2$ exhibits 33% crystallographic voids that range from 6 to 8 Å in diameter.¹⁷ Recently, we showed that small organometallic molecules like trimethylaluminum used in vapor-deposition techniques can infiltrate the pores of $\gamma\text{-Mg}(\text{BH}_4)_2$ to result in additives that diffuse into the bulk material rather than just depositing on the surface.¹⁸ The γ -phase transforms into higher density polymorphs of $\text{Mg}(\text{BH}_4)_2$ above $\sim 130\text{ }^{\circ}\text{C}$.¹⁹ Therefore, we have used vapor-phase precursors that can infiltrate the pores of $\gamma\text{-Mg}(\text{BH}_4)_2$ and react with $\text{Mg}(\text{BH}_4)_2$ well below $130\text{ }^{\circ}\text{C}$. Precursors that meet both criteria include BBr_3 (vdW radius = 3.3 Å), TiCl_4 (3.6 Å), and N_2H_4 (1.7 Å). This work will investigate the effects of the structure–morphology, chemistry, and hydrogen storage properties that these precursors have on $\gamma\text{-Mg}(\text{BH}_4)_2$. While the procedures of vapor-phase delivery (VPD) are identical with that of atomic layer deposition (ALD), the precursors infiltrate into the material beyond the surface and do not create a deposited coating; therefore, VPD verbiage is used in this article. Understanding how VPD affects these materials will be beneficial for the broader hydrogen storage community because this method of modification can introduce precise amounts of additives within the surface of metal hydride particles and can be scaled to large quantities. Compared to ball milling, VPD of additives for $\text{Mg}(\text{BH}_4)_2$ is an innocent additive deposition technique by controlling the number of cycles and avoiding undesired heating, mechanical transformation, or metal contamination.²⁰

Typically, metal hydride- and borohydride-based hydrogen storage materials are characterized with a suite of thermal, chemical, and crystallographic methods which include temperature-programmed desorption coupled with mass spectrometry (TPD-MS), Sieverts measurements, and X-ray diffraction (XRD). On very few occasions has electron microscopy characterization been used to study these complex metal hydride materials because they are generally air- and beam-sensitive, presenting both data acquisition and interpretation challenges.^{21,22} However, if carefully collected and interpreted, scanning transmission electron microscopy (STEM) paired with energy dispersive X-ray spectroscopy (EDS) mapping can provide essential visual clues for the evaluation of chemical and morphological phenomena occurring during the synthesis, hydrogen desorption, or hydrogen adsorption of Mg-based hydrogen storage materials. For example, Zhang et al. studied the decomposition of fluoride-doped $\text{Mg}(\text{BH}_4)_2$ by observing changes in the TEM diffraction pattern of the material while it was exposed to the electron beam.¹¹ Electron microscopy has also been used as a tool to locate chemical additives on hydride materials, demonstrate morphological changes in the hydrides after thermal decomposition, and identify specific hydride phases using electron diffraction.^{21,23–25} Additionally, two

recent reports were able to use STEM to examine the distribution of $\text{Mg}(\text{BH}_4)_2$ nanoconfined in MOFs and porous carbons after synthesis.^{26,27} However, this study specifically features STEM of pristine and modified $\text{Mg}(\text{BH}_4)_2$ as a bulk material rather than as a confined or modified entity, allowing for a comprehensive look into material morphology and elemental content and aiding the understanding of the changes occurring to the material through dehydrogenation. This study aims to demonstrate the benefits of performing identical location (IL)-STEM on metal hydrides before and after hydrogen desorption while providing thorough sample preparation and data interpretation considerations.

To summarize, this work demonstrates a vapor-phase approach to modifying $\text{Mg}(\text{BH}_4)_2$ materials that are comprehensively characterized using multiple complementary techniques. We present a thorough investigation of the pristine and modified materials before and after hydrogen desorption to elucidate the effect that the VPD modification has on the hydrogen desorption properties of $\gamma\text{-Mg}(\text{BH}_4)_2$. The study also demonstrates how the use of IL-STEM, while challenging, provides significant visual evidence of hydride materials before and after hydrogen desorption. The net result is a clearer picture of the complex chemistry occurring within these materials when using VPD.

METHODS

Materials Synthesis. The cubic $\gamma\text{-Mg}(\text{BH}_4)_2$ was synthesized using $\text{BH}_3\text{-S}(\text{CH}_3)_2$ and $\text{Mg}(\text{Bu})_2$ as the primary precursors, using the synthesis procedure reported by Zanella et al.⁴⁰ Full details of synthesis can be seen in a recent study by Schneemann et al. which utilizes a slightly modified version of the procedure.²⁶

Vapor-phase modification of $\gamma\text{-Mg}(\text{BH}_4)_2$ was performed with a Beneq TFS 200 ALD reactor. Samples were prepared, loaded, and unloaded inside a nitrogen glovebox directly interfaced with the ALD reactor to prevent exposure to air. $\gamma\text{-Mg}(\text{BH}_4)_2$ batches of $\sim 100\text{ mg}$ were loaded on a stainless steel wire cloth (325×3200 threads per inch) envelope and transferred into the reactor. VPD processes were conducted at $30\text{ }^{\circ}\text{C}$ and consisted of a precursor exposure (dose) followed by a purge to allow carrier gas to flush the reactor chamber of precursor vapor and products according to the sequence: precursor A dose–purge–precursor B dose–purge. One complete AB dose–purge sequence constitutes one “VPD” cycle. In all cases, the duration time of the dose and purge was 8 and 180 s, respectively. The “boron nitride” modification (BN-mod) used boron tribromide (BBr_3 , 99+%, Strem) and hydrazine (N_2H_4 , anhydrous 98%, MilliporeSigma), and the “titanium nitride” modification (TiN-mod) utilized titanium tetrachloride (TiCl_4 , 99%, Strem) and hydrazine. We selected BBr_3 because it is a liquid and is easier to handle for our experimental capabilities, but we hypothesize that the gases BCl_3 and BF_3 could be substituted. In all cases, a dose–purge of hydrazine was performed prior to the BN-mod or TiN-mod procedures in an attempt to remove surface oxides from the $\text{Mg}(\text{BH}_4)_2$ surface. Following a BN-mod the white $\text{Mg}(\text{BH}_4)_2$ powder had a flaky texture, and TiN-mod produced a color change that could range from yellow to green. From spectroscopy ellipsometry measurements, deposition of BN-mod and TiN-mod on silicon showed a linear dependence on the number of VPD cycles with a growth per cycle of 2 and 0.05 nm, respectively.

Temperature-Programmed Desorption (TPD). The samples studied in this work were analyzed on a calibrated, custom-built TPD system equipped with a Stanford Research Systems RGA 100, with $m/z = 1-100$ amu, sampling rate of 2–4 s, and 70 eV ionization energy. The samples were heated at a rate of 15 °C/min from 25 to 250 °C utilizing a Digi-Sense temperature controller. The quantity of material was adjusted to stay within the calibrated mass spectrometer's linear response region. In a typical analysis, 1–2 mg of sample was placed inside a platinum (Pt) foil packet to ensure homogeneous heating of the entire sample during the dehydrogenation process. The sample was then inserted into a quartz tube mounted to the TPD system without air exposure. All experimental parameters were controlled via a LabView interface with the RGA, heating system, and pressure gauges. Typical initial pressures before heating the sample are at 10^{-8} Torr, with a flat baseline, i.e., no water, hydrogen, or air signals above the background. Further information about the system was previously published.⁴¹ TPD data signals are all normalized to total sample mass which potentially includes the base $\text{Mg}(\text{BH}_4)_2$ and VPD-modified $\text{Mg}(\text{BH}_4)_2$.

Sieverts Method Measurements. Gravimetric H_2 capacity values were obtained without air exposure from the Sieverts method measurements on the Hy-Energy/Setaram PCT Pro 2000 for each sample presented in this work. The dehydrogenation was performed against vacuum at 200 °C, and the rehydrogenation was performed at 120 bar of H_2 and 280 °C. The sample mass used was 435 mg for uncoated $\text{Mg}(\text{BH}_4)_2$, and for the VPD-coated $\text{Mg}(\text{BH}_4)_2$ TiN-mod mass = 823 mg, BN-mod mass = 182 mg, BN-TiN-mod mass = 303 mg, and TiN-BN-mod mass = 329 mg.

X-ray Diffraction (XRD). XRD measurements were obtained at the Stanford Synchrotron Light Source (SSRL, SLAC National Accelerator Laboratory), beamline 7-2. Data were acquired with a Pilatus 100K area detector using X-rays with wavelength $\lambda = 0.8854$. The Debye–Scherrer geometry was used with transmission through 1.0 mm outer diameter (10 μm wall thickness) high-purity quartz capillaries open on both ends. The capillaries were loaded in an argon glovebox and mounted in the same sample cell without air exposure as was described by Hoffman et al.⁴² The 2D images were first normalized to incident beam intensity and subsequently integrated into a 1D pattern using an in-house Python-based program.

Scanning Transmission Electron Microscopy (STEM). STEM analysis was performed on a FEI Talos F200X instrument. Images were obtained in scanning mode with 200 keV accelerated voltage. EDS maps were created using Bruker EDS software and analysis was performed using standard protocols provided within this software. Materials were dispersed onto copper reference grids with carbon mesh (procured from Ted Pella, Inc.) in an argon atmosphere; dry preparation was employed to avoid any changes to the materials that could be introduced with exposure to the solvent. Prepared TEM grids were packaged in sealed aluminum packets for transport to the instrument. Once samples were removed from the package, they were immediately placed into the microscope and pumped down to the vacuum environment of the electron column. Time of air exposure was limited to the minimum, typically about 2 min between removal from packaging to the vacuum environment. At least 6 different particles were analyzed per sample and the location of all analyzed particles was noted for their identification and analysis after heating. The approximate beam dosage per image was $7.5 \text{ e}^- \text{ \AA}^{-2}$. After

initial TEM analysis, TEM grids with samples were removed from the holder and immediately brought to the glovebox, which resulted in an additional 4 min of air exposure. TEM grids with imaged samples were placed onto a temperature-monitored hot plate under an argon atmosphere and heated to 250 °C for 20 min. Once cooled, the samples were then packaged into airtight aluminum pouches for transport to the TEM and exposed to air for another 2 min while they were inserted into the TEM and pumped to the vacuum conditions, as discussed above. The total air exposure time for each sample was at maximum 8 min.

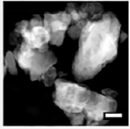
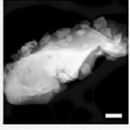
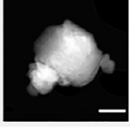
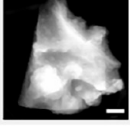
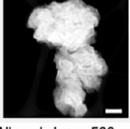
RESULTS

Materials Synthesis, Selection, and Initial Electron Microscopy. $\gamma\text{-Mg}(\text{BH}_4)_2$ samples were modified using VPD, with the intention of integrating different combinations of TiN and BN as chemical modifiers to the pristine borohydride. We hypothesize that the VPD technique will enable facile control of the interface between $\text{Mg}(\text{BH}_4)_2$ and additives, with the extent of chemical alteration based on the quantity and sequence of VPD cycles. Initial investigations resulted in over 12 combinations of sequences using the BN deposition (BN-mod) or TiN deposition (TiN-mod) processes, which are described in the experimental details. While many samples were produced, this paper highlights detailed characterization of four modified $\text{Mg}(\text{BH}_4)_2$ samples that demonstrated distinct effects of the BN-mod and the TiN-mod as well as the effect of the two modifying procedures when used in combination. The selected samples for discussion in this work are presented with summarized synthetic procedures in Figure 1.

All samples were imaged using high angle annular dark field (HAADF) STEM (Figure 1). The neat $\text{Mg}(\text{BH}_4)_2$ synthesis exhibits slight variation in morphology and composition but can be classified as a porous material with a broad particle size distribution (200 nm to several micrometers in diameter). The porosity of $\text{Mg}(\text{BH}_4)_2$ is supported by N_2 physisorption analysis at 77 K which is provided in Figure S1. The morphology of the materials after VPD modification generally remains similar to that of the neat material. STEM images included in this study are representative of each sample; however, variation does exist across the particles. It must also be noted that the VPD-BN sample produces particles that are too large to be imaged by TEM; therefore, a sample that is only exposed to 10 cycles of BN-mod is imaged in its place. Variations in brightness within the neat $\text{Mg}(\text{BH}_4)_2$ material suggest slight variations in density and/or particle depth, which is consistent for each modified sample in this set. The next sections of this work present measurements that assess hydrogen storage properties of synthesized samples as well as further discussion of the nature of the VPD modification.

Gas Desorption. The hydrogen desorption behavior of the VPD-modified $\text{Mg}(\text{BH}_4)_2$ was studied with TPD-MS and Sieverts method measurements. TPD-MS indicates the gas-phase products released during thermolysis, and the manometric Sieverts method measurements quantifies the gaseous products evolved during thermolysis. Figure 2 demonstrates the hydrogen release during TPD for the selected samples and has been normalized to sample mass which allows for comparison of signal intensity.

The neat material shows very little desorption up to 300 °C, as expected.²⁸ In contrast, the VPD-BN sample desorbs a large amount of H_2 at 120 °C, which is distinguished by a sharp signal and is characteristic for all samples when BN-mod was introduced first to form the interface with the $\text{Mg}(\text{BH}_4)_2$. This

Sample Name (Identifier)	VPD: 10 Cycles	VPD: 100 cycles	STEM (HAADF)
γ -Mg(BH ₄) ₂ (Neat)	N/A	N/A	
γ -Mg(BH ₄) ₂ - 100cBN** (VPD-BN)	N/A	8s N ₂ H ₄ 180s N ₂ 8s BBr ₃	
γ -Mg(BH ₄) ₂ - 100cTiN (VPD-TiN)	N/A	8s N ₂ H ₄ 180s N ₂ 8s TiCl ₄	
γ -Mg(BH ₄) ₂ - 10cBN- 100cTiN (VPD-BN-TiN)	8s N ₂ H ₄ 180s N ₂ 8s BBr ₃	8s N ₂ H ₄ 180s N ₂ 8s TiCl ₄	
γ -Mg(BH ₄) ₂ - 10cTiN- 100cBN (VPD-TiN-BN)	8s N ₂ H ₄ 180s N ₂ 8s TiCl ₄	8s N ₂ H ₄ 180s N ₂ 8s BBr ₃	

All scale bars: 500nm

Figure 1. Sample names are presented here with their respective synthetic vapor exposures. On the right-hand column, STEM micrographs of representative particles are presented. **It must be noted that the imaged VPD-BN sample presented in this figure has only been exposed to 10 cycles of BN-mod, as the 100c BN-mod particles were too large to image with TEM.

signal at 120 °C is extremely intense as well as sharp and quickly diminishes. In contrast, VPD-TiN does not demonstrate this low-temperature desorption but gradually desorbs H₂ as the sample is heated to high temperatures. Interestingly, the VPD-BN-TiN sample can desorb hydrogen at 100 °C, an even lower temperature than VPD-BN, and continues to release significant amounts of H₂ up to 300 °C. However, the same effect is not seen for the VPD-TiN-BN (where TiN-mod is introduced prior to BN-mod), which releases only a small amount of H₂ by comparison to its counterpart and appears to release H₂ in a mechanism that is more similar to VPD-TiN. This suggests that the reaction occurring within Mg(BH₄)₂ during BN-mod is critical to enable rapid release of hydrogen from Mg(BH₄)₂ at low temperatures.

Hydrogen is the major gaseous product formed during dehydrogenation for the materials discussed in this work. Figure S2 shows the complete mass spectra for the TPD measurements, demonstrating both H₂ and other byproducts released at significantly lower quantities, usually about 2 orders of magnitude less than hydrogen. Figure 3 presents the selected *m/z* signals from H₂, N₂, and B₂H₆ for each sample. VPD-BN (Figure 3a) shows a small peak in N₂ signal that coincides with H₂ release but is about 3 orders of magnitude less, while diborane signal remains minimal throughout heating. In the VPD-TiN, VPD-BN-TiN, and VPD-TiN-BN samples, N₂ and B₂H₆ both track fairly well with each other, in a desorption pattern that follows the general shape of the H₂ trace, but at orders of magnitude less than H₂. The TPD of VPD-BN-TiN (Figure 3c) shows the increase of B₂H₆ and N₂ signal after the

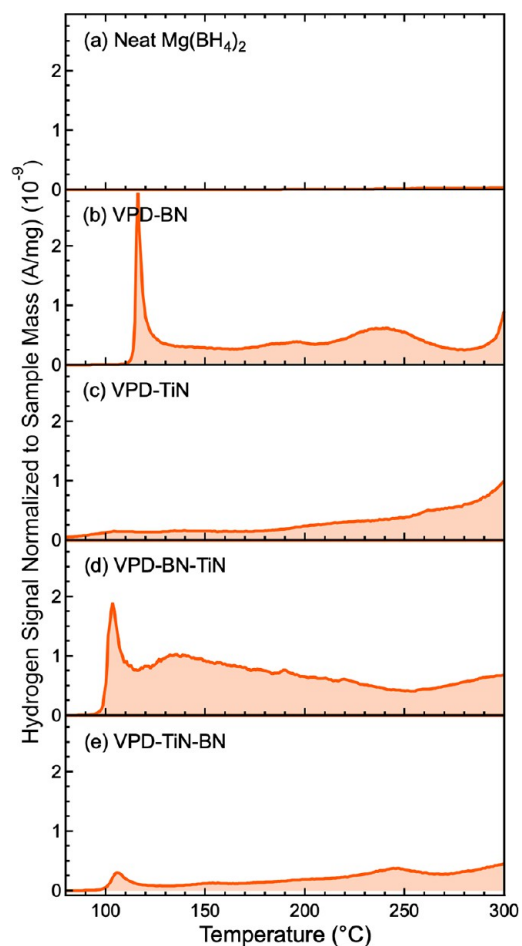


Figure 2. Hydrogen release as determined by TPD of (a) neat Mg(BH₄)₂, (b) VPD-BN, (c) VPD-TiN, (d) VPD-BN-TiN, and (e) VPD-TiN-BN.

initial spike of hydrogen release (from 125 to 175 °C). This increase in byproduct signal demonstrates how the mechanism of desorption for this sample may be a two-step process of an initial release that triggers a second desorption above 125 °C.

Multiple H₂ desorption–absorption cycles were performed on all modified materials. The conditions for the H₂ cycles did not exceed 250 °C, and H₂ absorption occurred under 120 bar of H₂. Figure 4 shows the results for the first cycle, and the complete cycling behavior can be found in Figure S3. Hydrogen desorption in these plots is represented with a negative sign and shown in blue, whereas absorption is positive and shown in pink. The VPD-BN material (Figure 4b) shows rapid desorption, where −6.6 wt % hydrogen is released in <10 s which gives the distinct boxlike desorption curve. VPD-BN-TiN (Figure 4d) also shows low-temperature, rapid desorption, albeit not as fast as the VPD-BN material, and a larger desorbed amount of hydrogen of −7.6 wt %. The VPD-TiN (Figure 4c) showed steady desorption until it eventually reached −3.0 wt % hydrogen. VPD-TiN-BN (Figure 4e) also showed improved hydrogen desorption compared to the uncoated material with a release of −2.2 wt % hydrogen. Thus, all of the VPD-treated materials showed greater desorption rates than the neat Mg(BH₄)₂, which released −1.7 wt % hydrogen (Figure 4a).

Hydrogen absorption behavior of these materials did not match the rapid rates or large quantities observed for hydrogen desorption. The respective absorbed hydrogen can be seen in

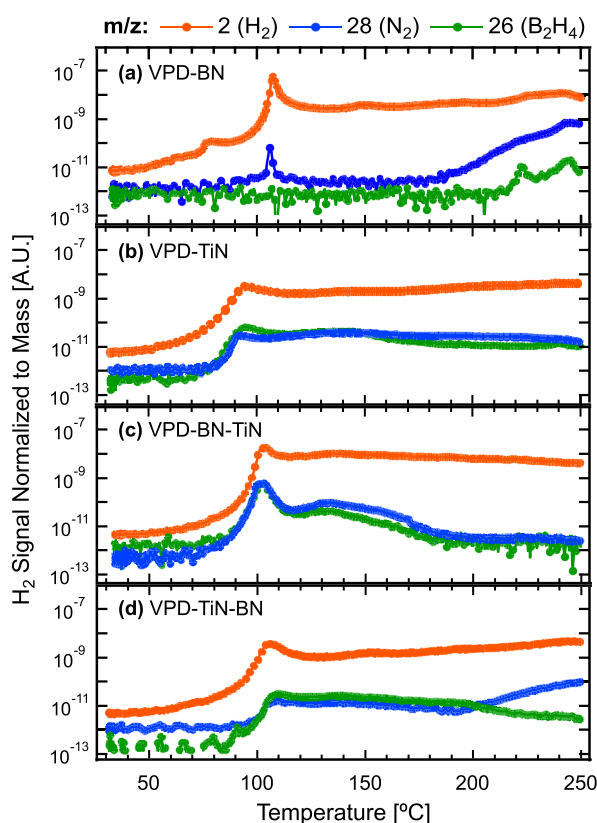


Figure 3. TPD mass spectra of (a) VPD-BN, (b) VPD-TiN, (c) VPD-BN-TiN, and (d) VPD-TiN-BN. The hydrogen signal ($m/z = 2$) is reported for all cases in orange, diborane ($m/z = 26$) in green, and nitrogen ($m/z = 28$) in blue.

Figure 4 in pink; +0.5, +1.9, +1.1, +0.2, and +0.4 wt % hydrogen were absorbed for the neat $\text{Mg}(\text{BH}_4)_2$, VPD-BN, VPD-TiN, VPD-BN-TiN, and VPD-TiN-BN samples, respectively.

Subsequent desorption–absorption cycles resulted in comparatively low capacities and rates (see Table S1), as expected due to low absorption. Only VPD-BN showed promise of cyclability at these conditions where -1.2 wt % hydrogen was desorbed in the second desorption cycle. The rest of the materials cycled poorly, with generally less than ± 0.5 wt % hydrogen desorbed–absorbed.

X-ray Diffraction. XRD was used to determine the structural changes to $\gamma\text{-Mg}(\text{BH}_4)_2$ after VPD modification and compared to the neat $\gamma\text{-Mg}(\text{BH}_4)_2$ reference (Figure 5). Compared to unmodified $\gamma\text{-Mg}(\text{BH}_4)_2$, relative intensities from the γ -phase reflections and higher background counts are indicative of a surface reaction that reduces the amount of crystalline material, forming amorphous content. Interestingly, the VPD-BN also shows the presence of hydrazinium monobromide, $\text{N}_2\text{H}_5\text{Br}$, which is formed during the reaction of N_2H_4 and BBr_3 shown previously by Paterson et al.³³ The VPD-TiN scan reveals higher intensity reflections from $\gamma\text{-Mg}(\text{BH}_4)_2$ than VPD-BN; however, additional peaks illustrate the formation of α -phase $\text{Mg}(\text{BH}_4)_2$ in this sample. Although both modified samples exhibit diminished $\gamma\text{-Mg}(\text{BH}_4)_2$ peaks relative to the unmodified material, they both demonstrate that the bulk material is at least partially retained after VPD modification. XRD data for VPD-TiN-BN and VPD-BN-TiN are shown in Figures S4 and S5. Although γ - and α - $\text{Mg}(\text{BH}_4)_2$ are identified in the XRD data for the VPD-TiN-BN and VPD-BN-TiN combination samples, $\text{N}_2\text{H}_5\text{Br}$ was not observed.

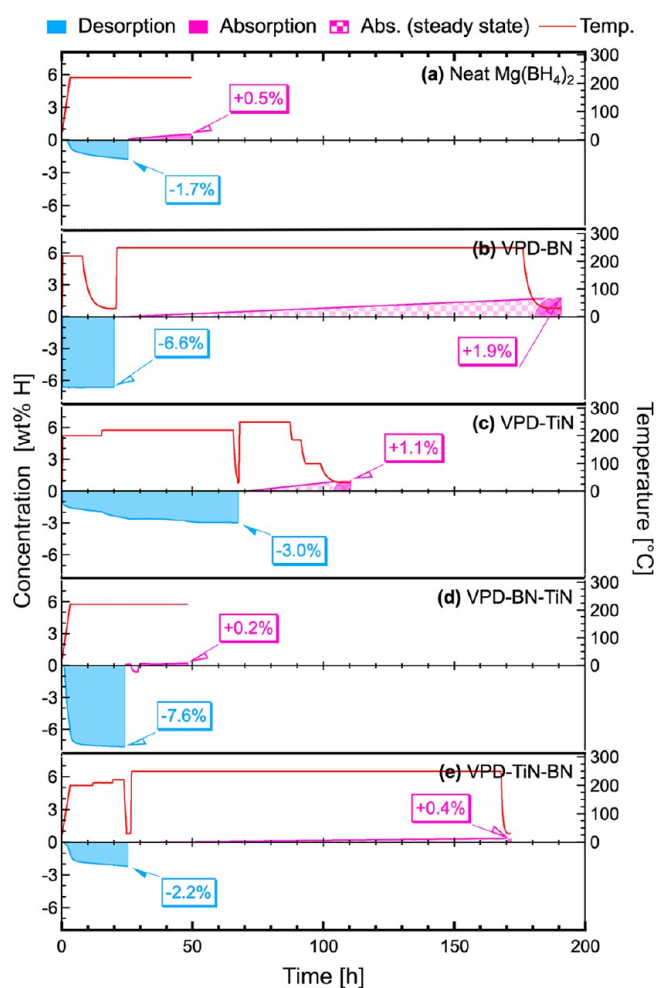


Figure 4. PCT measurements on each of the selected samples. Blue curves represent hydrogen desorption while pink notation denotes absorption of hydrogen. The red line on each graph shows the temperature of the sample and is referenced on the right axis.

Identical Location Microscopy. IL-STEM was collected on each sample before and after thermal hydrogen desorption to better understand how different VPD modifications affect the morphology and composition transformation of $\text{Mg}(\text{BH}_4)_2$ during hydrogen release (see Figure 6). The size, composition, and morphology of the particles of the neat material vary significantly, which means that conclusions based on comparisons of different particles before and after hydrogen desorption could be misleading. To make more conclusive comparisons before and after hydrogen, IL microscopy was performed on selected particles of similar sizes across the sample set. Selecting particles of a similar size and observing the differences within these particles after heating mitigated some of the uncertainty of analyzing these complex, heterogeneous materials.²²

IL microscopy was performed by selecting and imaging individual particles of as-synthesized samples on a referenced TEM grid, which was then removed from the microscope, and brought to a glovebox where the sample was heated to 250°C under an argon atmosphere. Then the TEM grid was placed back into the microscope, and the same particles are located and imaged again. In Figure 6, HAADF images highlight morphological changes in the material before and after heating to 250°C and are presented along with EDS maps and atomic composition charts of selected elements (see corresponding

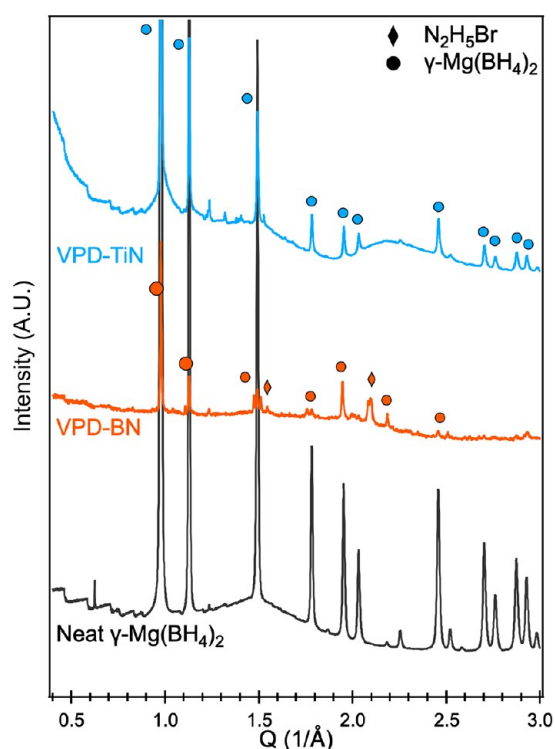


Figure 5. XRD of (a) neat γ - $\text{Mg}(\text{BH}_4)_2$, (b) VPD-BN, and (c) VPD-TiN. Peaks corresponding to γ - $\text{Mg}(\text{BH}_4)_2$ (denoted with circles) are present in VPD-modified materials but diminished significantly.

labels in Figure 6). Each EDS map has a consistent color scheme where the element of interest is seen in pink while magnesium is always shown in yellow, avoiding misinterpretation of different color combinations falsely suggesting a more prominent element. To the right of the EDS maps, Figure 6 provides a qualitative atomic percentage of each element present in these samples. Because of oxidation of the reactive species during exposure to air, there is a large quantity of oxygen present in these samples before and after hydrogen desorption. The complete summary of the elemental compositions (including oxygen maps) of the series can be found in Figure S6; however, oxygen is omitted from the presented data in Figure 6 to better visualize changes in the elements of lower quantities.

The inherent flaw in this method of IL-STEM comes from the logistics of requiring short periods (<5 min) of air exposure during transfer of samples to and from the instrument. This exposure increased oxygen content and slightly reduced boron content detected by EDS due to the release of diborane in air. Additionally, boron is systematically underrepresented in EDS quantities due to its low-energy photons frequently absorbing into surrounding material before they are detected.²⁹ Because of the possible effects associated with the limited oxygen exposure, and low boron counts, it is advised that EDS as presented in this paper is not treated as quantitative data but rather as a method of determining qualitative trends of elemental composition before and after heating for individual materials as well as across the set of samples. Nevertheless, the use of IL-STEM improved the reliability of observed trends compared to imaging separate samples prior to and after hydrogen desorption. Because air exposure was consistent for all studied samples, morphological and elemental trends could be determined using IL-STEM and compared with other physical characterization techniques to make conclusions about the effects of VPD on each sample.

The neat $\text{Mg}(\text{BH}_4)_2$ sample (Figure 6a) is the only material that expanded after heating (ImageJ-quantified 2-D particle areas can be seen in Figure S7).³⁰ The darker or “more hollow” appearance of this sample implies a less dense sample with higher probability for electrons to pass through the sample during imaging. The apparent decrease in density suggests $\text{Mg}(\text{BH}_4)_2$ decomposition and phase changes from both heating the sample to 250 °C and electron beam exposure.²⁰ EDS of the neat $\text{Mg}(\text{BH}_4)_2$ before and after heating is unsurprising and demonstrates signals mainly from magnesium and boron, with the exception of oxygen from air exposure.

Figure 6b shows images of a sample of $\text{Mg}(\text{BH}_4)_2$ after only 10 BN-mod cycles in place of the 100 cycle counterpart that was analyzed in the TPD, PCT, and XRD and is denoted as VPD-10BN. This sample was imaged rather than VPD-BN because BN-mod grows much faster than TiN-mod (2 nm/cycle vs 0.5 nm/cycle, respectively) and resulted in particles that were too large to image using TEM. This also allowed for characterization of the material before significant $\text{Mg}(\text{BH}_4)_2$ decomposition occurs (as can be seen in Figure 5b). After heating, this sample generally demonstrated a small decrease in size and dark field signal, similar to what is observed for the neat $\text{Mg}(\text{BH}_4)_2$ material, suggesting a smaller, less dense material. Before dehydrogenation, VPD-10BN looks very similar to the neat sample but with a notable increase of bromine near the surface of the material. After heating, bromine levels decreased and were no longer detected on the outer shell of the particle in the EDS map.

The third sample presented in Figure 6c is VPD-TiN, which appears denser than other samples due to the brightness of the HAADF signal. After heating, this sample remains dense, and the volume of the particles decreases only slightly (see Figure S7 for particle volume changes). From the EDS maps and quantification, one can see that nitrogen is present throughout the whole particle, while chlorine is detected only at the surface. After heating to 250 °C, the elemental composition does not change drastically except for a small decrease in the amount of chlorine seen near the edges of the particle.

VPD-BN-TiN released the most hydrogen (−7.6 wt %) of all the samples and HAADF images show a significant decrease in size and density after hydrogen release (seen in Figure 6d). It is noted that there are some bright spots seen on the heated sample which are an artifact of copper migration from the TEM grid onto the samples during the heating process. Elemental analysis of the as-synthesized particle demonstrates integration of nitrogen throughout the material, especially in locations where titanium is also present. This suggests that N_2H_4 is infiltrating into the $\text{Mg}(\text{BH}_4)_2$ and reacting with the TiCl_4 precursor, which is discussed further in the Discussion section of this paper. Both chlorine and bromine are present in these particles at high percentages, which signifies that the bromine and chlorine are entering into the pore space of $\text{Mg}(\text{BH}_4)_2$ during reaction of the BBr_3 and TiCl_4 precursors, respectively. After heating to 250 °C, nitrogen, chlorine, and bromine all decrease in atomic percent, suggesting that they may play a role in the low-temperature desorption of hydrogen.

VPD-TiN-BN demonstrated the greatest particle size reduction and appears denser after heating to 250 °C, which can be seen in Figure 6e. This reduction in size and increase in density could be due to a phase change from γ - $\text{Mg}(\text{BH}_4)_2$ to β - $\text{Mg}(\text{BH}_4)_2$.³¹ In the as-synthesized VPD-TiN-BN, an increased amount of bromine is observed, albeit, in the absence of nitrogen or chlorine incorporation. While the atomic percentage of

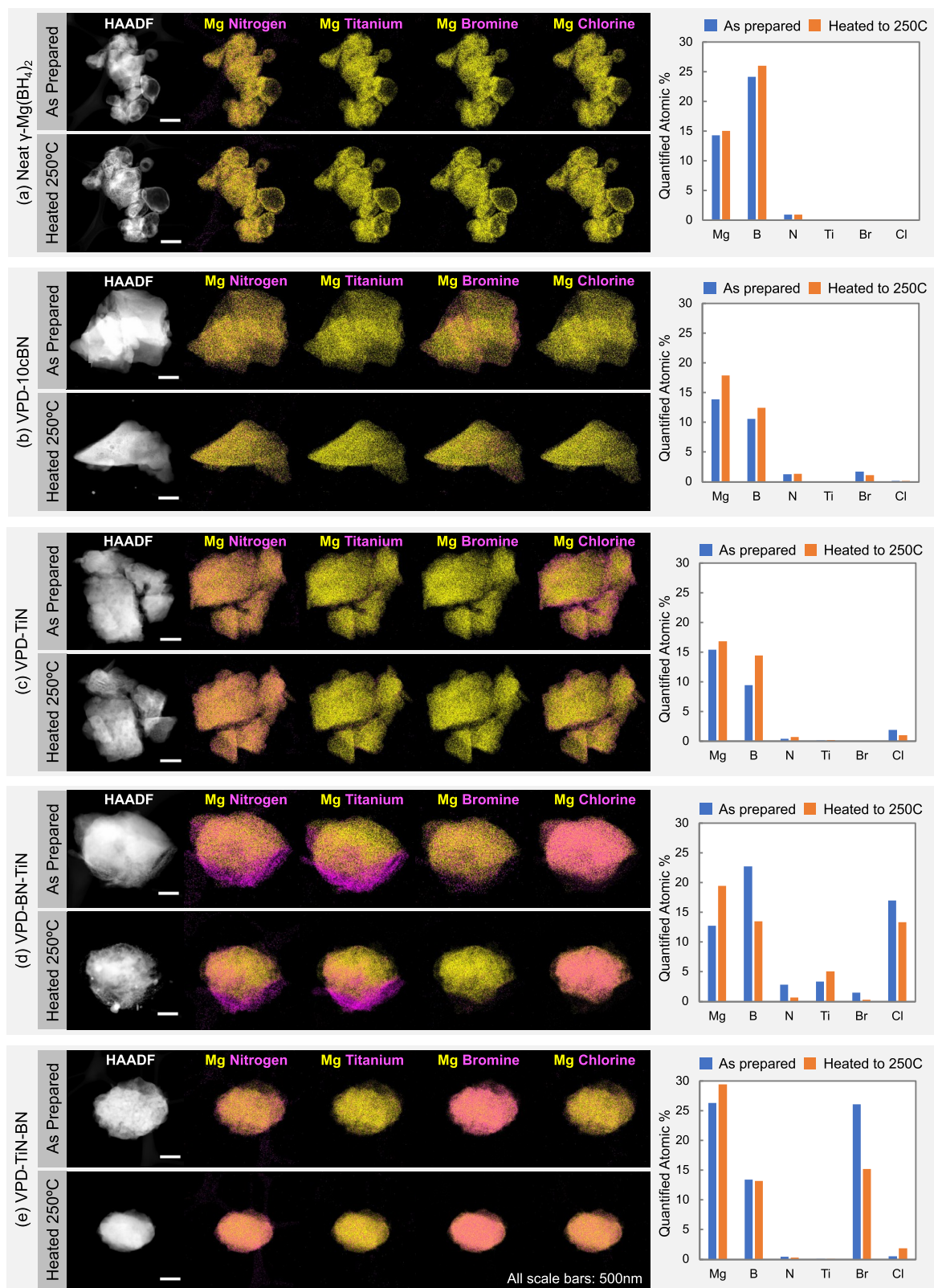


Figure 6. STEM-EDS identical location analysis of (a) neat Mg(BH₄)₂, (b) VPD-BN (with only 10 BN-mod cycles), (c) VPD-TiN, (d) VPD-BN-TiN, and (e) VPD-TiN-BN. Figure includes HAADF images (left) and EDS map overlays of individual particles before (top) and after heating to 250 °C (bottom). Yellow is used to depict magnesium to show the material base while pink is used to show elements introduced via VPD: N, Ti, Br, and Cl. Using the same color across all elements highlights differences between samples and additives. To the right of STEM images, EDS quantification of each element's atomic percentage is presented, with the exception of oxygen quantification which can be found in Figure S6.

bromine does decrease after dehydrogenation, similar to VPD-BN-TiN, the performance is not nearly as impressive. This

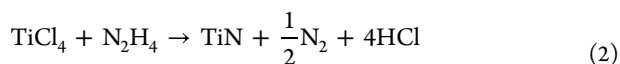
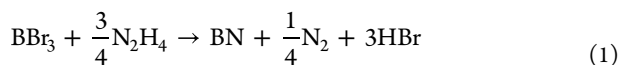
suggests that the bromine is necessary for low-temperature desorption, but not the main source of large hydrogen

desorption quantities. It is also noted that the VPD-TiN-BN sample with 100 cycles of BN does not grow as large as the VPD-BN sample, which was too large to image. It is hypothesized that the surface modification that occurs during TiN deposition alters the reaction mechanism of BN-mod and reduces the growth rate on this sample.

DISCUSSION

On the basis of all characterizations of VPD-modified materials presented above, it is clear that the hydrogen release mechanism is not a direct one-step decomposition of $\text{Mg}(\text{BH}_4)_2$ facilitated by VPD modifications, as was originally hypothesized. The following section provides discussion of the chemistry that is likely occurring within the surface of $\text{Mg}(\text{BH}_4)_2$ during VPD and desorption processes, while also acknowledging that not all of the questions about these complex processes can be answered at this time. The desorption mechanism of the VPD-modified samples promotes the release of hydrogen at temperatures well below that of neat $\text{Mg}(\text{BH}_4)_2$ under normal conditions which desorbs at approximately 300 °C.^{19,32} An initial hypothesis that N_2H_4 alone was responsible for this low-temperature desorption was proven incorrect after TPD analysis of a sample exposed to 100 doses of N_2H_4 resulted in almost an order of magnitude less hydrogen release at a higher temperature than VPD-BN (Figure S8). This points to the importance of combining N_2H_4 with the BBr_3 precursors as the first vapor modification to release hydrogen at lower temperatures. In samples where BN-mod was used initially, the presence of nitrogen and bromine in STEM/EDS after VPD modification as well as the detection of crystalline $\text{N}_2\text{H}_5\text{Br}$ from XRD leads to the likelihood that $\text{N}_2\text{H}_5\text{Br}$ is formed with the combination of these precursors.

We propose that because vapor modification occurred at a low temperature (30 °C) and $\gamma\text{-Mg}(\text{BH}_4)_2$ is a porous structure, HBr or HCl from eqs 1 and 2 could linger within the pores of $\gamma\text{-Mg}(\text{BH}_4)_2$ through subsequent hydrazine exposures.

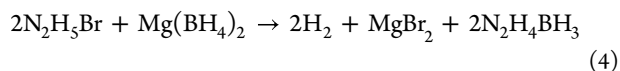


Remnant HX species were then available to react with the hydrazine exposures to form hydrazinium halides, as was reported by Paterson and Onyszchuk



where X = F, Cl, Br, or I.³³

The presence and close proximity of protic hydrogen ($\text{H}^{\delta+}$) of N-H at the surface from $\text{N}_2\text{H}_5\text{Br}$ with the hydridic hydrogen ($\text{H}^{\delta-}$) in B-H in the $\text{Mg}(\text{BH}_4)_2$ supports a heterolytic bond cleavage to give the following metathesis reaction during the thermal decomposition of VPD-BN:



where eq 4 is based on similar reactions that form hydrazine borane ($\text{N}_2\text{H}_4\text{BH}_3$) and has the $\text{N}-\text{H}^{\delta+} \text{B}-\text{H}^{\delta-}$ mechanism that would enable the rapid, low-temperature desorption.^{34,35} In the case of VPD-BN-TiN, it is assumed that the same $\text{N}_2\text{H}_5\text{Br}$ product is formed during the BN-mod cycles. However, the $\text{TiCl}_4 + \text{N}_2\text{H}_4$ modifications also introduce chlorine to the $\text{N}_2\text{H}_5\text{Br}$ species, which could spontaneously undergo anion replacement to generate $\text{N}_2\text{H}_5\text{Cl}$ due to the higher electro-

negativity of chlorine compared to bromine. This is supported by a significant increase of the chlorine signal in the EDS of this sample (Figure 6d). The hydrogen yield for eq 4 would only be 1.4 wt %, and an analogous reaction with $\text{N}_2\text{H}_5\text{Cl}$ would produce 2.1% hydrogen. The yield of 6–7 wt % hydrogen for the VPD materials means that the $\text{N}-\text{H}^{\delta+} \text{B}-\text{H}^{\delta-}$ mechanism may trigger additional reactions such as decomposition of hydrazine borane or desorption from $\text{Mg}(\text{BH}_4)_2$ that was not directly affected by the VPD process. Because of this, a subsequent publication is being developed that will apply additional characterization to capture the complete desorption process for these materials.

The VPD-TiN materials desorb hydrogen at temperatures lower than unmodified $\text{Mg}(\text{BH}_4)_2$, but the effects of the VPD process are less straightforward. Room temperature XRD scans of VPD-TiN, seen in Figure 5c, show much more defined $\text{Mg}(\text{BH}_4)_2$ peaks than the VPD-BN counterpart, providing evidence of more intact $\text{Mg}(\text{BH}_4)_2$ structures after TiN-mod. EDS quantification (Figure 6c) indicates the presence of nitrogen and chlorine within the VPD-TiN sample. A metathesis reaction between TiCl_4 and $\text{Mg}(\text{BH}_4)_2$ to produce volatile $\text{Ti}(\text{BH}_4)_3$ or $\text{TiCl}(\text{BH}_4)_2$ products could explain the low titanium levels (see the Supporting Information for reaction schemes).^{35–37} Anion exchange between BH_4^- and Cl^- ions to yield a solid solution $\text{Mg}(\text{BH}_4)_{2-x}\text{Cl}_x$ was also reported previously by Hino et al.³⁸ A vapor phase anion exchange for $\gamma\text{-Mg}(\text{BH}_4)_2$ would be interesting because the authors used ball milling and found that only the beta phase supports anion exchange. A $\text{Mg}(\text{BH}_4)_{2-x}\text{Cl}_x$ compound would explain the higher counts of chlorine relative to nitrogen measured with EDS for the 100cTiN sample. This phenomenon has also been suggested by Strange et al., where $\gamma\text{-Mg}(\text{BH}_4)_2$ exposed to 100 doses of TiCl_4 precursor yielded no secondary boron environments (i.e., BH_4^- remained intact) and spectroscopic evidence of MgCl_2 on the surface of the modified material.³⁸ Further evidence for anion exchange in the VPD-TiN is provided by *in situ* XRD, which shows diffraction from MgCl_2 at 200 °C, i.e., the fully exchanged product (see Figure S9). Interestingly, the TPD from VPD-TiN is nearly identical with that observed from the $\text{TiCl}_4\text{-Mg}(\text{BH}_4)_2$ sample presented by Strange et al. As discussed above, a deeper investigation of these phenomena is being developed to address the complete process of desorption. However, it is apparent that the key factor causing rapid, low-temperature production of hydrogen is direct contact between the VPD-BN precursors and $\gamma\text{-Mg}(\text{BH}_4)_2$.

In our initial efforts, we did not find the release of bromine or chlorine products in TPD that could explain the significant decrease in chlorine and bromine seen in IL-STEM/EDS after dehydrogenation (Figure 3). The authors recommend further microscopy studies that include an environmental *in situ* STEM experiment, which would eliminate the inherent flaw of air exposure that IL-STEM introduces in this study. However, while an *in situ* STEM study would allow for analysis of the material without oxygen exposure, one must also be aware of the potential issues associated with loss in EDS signal from obstruction of the X-ray from the *in situ* holder geometry.³⁹ A following investigation will apply spectroscopy, XRD, and other characterization as a function of temperature to identify reaction products throughout the process.

CONCLUSIONS

Gamma phase $\text{Mg}(\text{BH}_4)_2$ was modified using scalable VPD methods to yield several potential hydrogen storage materials. This paper discusses the mechanism of VPD modification and

hydrogen release for each material presented here due to the combined power of several characterization techniques including TPD, Sieverts, XRD, and IL-TEM. The combination of XRD and IL-STEM identified hydrazinium bromide, observed a lower than expected level of titanium, and led to proposing a possible chloride exchange with both the borohydride and hydrazinium bromide. Although none of the VPD-modified $\text{Mg}(\text{BH}_4)_2$ samples satisfy the stringent requirements for rechargeable hydrogen storage, this study demonstrates the utility of VPD techniques to efficiently introduce various additives into high-capacity metal hydrides. Our studies also provide important mechanistic insights into the changes in reactivity and morphology of $\text{Mg}(\text{BH}_4)_2$ by VPD processes, accompanied by a significant reduction in the hydrogen desorption temperature and enhancement of the reaction rates. The vapor phase modified materials demonstrate low-temperature, rapid, pure hydrogen release of 6–8 wt % hydrogen through an irreversible combination of partially charged hydrogens from $\text{Mg}(\text{BH}_4)_2$ and $\text{N}_2\text{H}_5\text{Br}$ which yields a mixture of products. While these specific VPD combinations on $\text{Mg}(\text{BH}_4)_2$ did not produce a rechargeable hydrogen storage material, this study provided great insight into how VPD provides a complete coating and interaction with all surfaces of porous hydrides. Additionally, the rapid, low-temperature release of high-capacity hydrogen in our BN-modified gamma phase $\text{Mg}(\text{BH}_4)_2$ demonstrates a possible pathway to an alternative hydrogen storage material.

■ ASSOCIATED CONTENT

SI Supporting Information

The Supporting Information is available free of charge at <https://pubs.acs.org/doi/10.1021/acs.jpcc.2c04777>.

Figure S1: pore size analysis of neat $\text{Mg}(\text{BH}_4)_2$; Figure S2: full mass spectra from TPD analysis of each VPD combination presented in this work; Figure S3: the Sieverts method H_2 cycling data for each sample discussed in the text as well as (Table S1) the numerical values obtained from this measurement; Figure S4: XRD data from VPD-TiN, VPD-TiN-BN, and VPD-TiN-BN heated to 250 °C; Figure S5: XRD data from VPD-BN, VPD-BN-TiN, and VPD-BN-TiN heated to 250 °C; Figure S6: quantification results from EDS including oxygen with oxygen maps; Figure S7: the particle size differences for each sample in this work based on area analysis of TEM images before and after hydrogen desorption; Figure S8: TPD analysis of VPD-BN compared with a sample only dosed with N_2H_2 ; Figure S9: *in situ* XRD data of VPD-TiN during heating under dynamic vacuum and a proposed metathesis reaction of TiCl_4 and $\text{Mg}(\text{BH}_4)_2$ (PDF)

■ AUTHOR INFORMATION

Corresponding Authors

Svitlana Pylypenko – Department of Chemistry, Colorado School of Mines, Golden, Colorado 80401, United States; orcid.org/0000-0001-7982-734X; Email: spylypen@mines.edu

Noemi Leick – National Renewable Laboratory, Golden, Colorado 80401, United States; orcid.org/0000-0002-2014-6264; Email: noemi.leick@nrel.gov

Authors

Margaret Fitzgerald – Department of Chemistry, Colorado School of Mines, Golden, Colorado 80401, United States; orcid.org/0000-0003-2976-0145

Sarah Shulda – National Renewable Laboratory, Golden, Colorado 80401, United States

Nicholas A. Strange – SLAC National Accelerator Laboratory, Menlo Park, California 94025, United States; orcid.org/0000-0001-5699-7274

Andreas Schneemann – Sandia National Laboratories, Livermore, California 94551, United States; orcid.org/0000-0001-6801-2735

Vitalie Stavila – Sandia National Laboratories, Livermore, California 94551, United States; orcid.org/0000-0003-0981-0432

Liwen F. Wan – Lawrence Livermore National Laboratory, Livermore, California 94551, United States; orcid.org/0000-0002-5391-0804

Karl Gross – H2Technology Consulting, Alamo, California 94507, United States

Thomas Gennett – Department of Chemistry, Colorado School of Mines, Golden, Colorado 80401, United States; National Renewable Laboratory, Golden, Colorado 80401, United States

Steven Christensen – National Renewable Laboratory, Golden, Colorado 80401, United States

Complete contact information is available at: <https://pubs.acs.org/doi/10.1021/acs.jpcc.2c04777>

Notes

The authors declare no competing financial interest.

■ ACKNOWLEDGMENTS

This paper describes objective technical results and analysis. Any subjective views or opinions that might be expressed in the paper do not necessarily represent the views of the U.S. Department of Energy or the United States Government. The authors gratefully acknowledge research support from the Hydrogen Materials - Advanced Research Consortium (HyMARC), established as part of the Energy Materials Network under the U.S. Department of Energy, Office of Energy Efficiency and Renewable Energy, Hydrogen Fuel Cell Technologies Office, under Contract DE-AC36-08GO28308. Sandia National Laboratories is a multimission laboratory managed and operated by National Technology and Engineering Solutions of Sandia, LLC., a wholly owned subsidiary of Honeywell International, Inc., for the U.S. Department of Energy's National Nuclear Security Administration (NNSA) under Contract DE-NA-0003525. Use of the Stanford Synchrotron Radiation Light-source, SLAC National Accelerator Laboratory, is supported by the U.S. Department of Energy, Office of Science, Office of Basic Energy Sciences, under Contract DE-AC02-76SF00515. A portion of the research was performed using EMSL (grid.436923.9), a DOE Office of Science User Facility sponsored by the Office of Biological and Environmental Research. This work was performed under the auspices of the U.S. Department of Energy by Lawrence Livermore National Laboratory (LLNL) under Contract DE-AC52-07NA27344. The authors thank Thomas Autrey and Mark Bowden at the Pacific Northwest National Laboratory for facilitating access to the EMSL facilities.

REFERENCES

- (1) H2@Scale | Department of Energy <https://www.energy.gov/eere/fuelcells/h2scale> (accessed 2020-10-06).
- (2) Energy Storage Grand Challenge Roadmap | Department of Energy <https://www.energy.gov/energy-storage-grand-challenge/energy-storage-grand-challenge/> (accessed 2021-02-23).
- (3) Bundesministerium für Wirtschaft und Energie. Die Nationale Wasserstoffstrategie, 2020.
- (4) Baykara, S.; Hydrogen, Z. A Brief Overview on Its Sources, Production and Environmental Impact. *Int. J. Hydrogen Energy* **2018**, *43* (23), 10605–10614.
- (5) Yartys, V. A.; Lototsky, M. V.; Akiba, E.; Albert, R.; Antonov, V. E.; Ares, J. R.; Baricco, M.; Bourgeois, N.; Buckley, C. E.; Bellosta von Colbe, J. M.; et al. Magnesium Based Materials for Hydrogen Based Energy Storage: Past, Present and Future. *Int. J. Hydrogen Energy* **2019**, *44* (15), 7809–7859.
- (6) Rusman, N. A. A.; Dahari, M. A Review on the Current Progress of Metal Hydrides Material for Solid-State Hydrogen Storage Applications. *Int. J. Hydrogen Energy* **2016**, *41* (28), 12108–12126.
- (7) Newhouse, R. J.; Stavila, V.; Hwang, S.-J.; Klebanoff, L. E.; Zhang, J. Z. Reversibility and Improved Hydrogen Release of Magnesium Borohydride. *J. Phys. Chem. C* **2010**, *114* (11), S224–S232.
- (8) Zavorotynska, O.; El-Kharbachi, A.; Deledda, S.; Hauback, B. C. Recent Progress in Magnesium Borohydride Mg(BH₄)₂: Fundamentals and Applications for Energy Storage. *Int. J. Hydrogen Energy* **2016**, *41* (32), 14387–14403.
- (9) Huot, J.; Liang, G.; Schulz, R. Mechanically Alloyed Metal Hydride Systems. *Appl. Phys. A: Mater. Sci. Process.* **2001**, *72*, 187–195.
- (10) Oelerich, W.; Klässen, T.; Bormann, R. Metal Oxides as Catalysts for Improved Hydrogen Sorption in Nanocrystalline Mg-Based Materials. *Journal of Alloys and Compounds* **2001**, *315*, 237–242.
- (11) Zhang, Z. G.; Wang, H.; Liu, J. W.; Zhu, M. Thermal Decomposition Behaviors of Magnesium Borohydride Doped with Metal Fluoride Additives. *Thermochim. Acta* **2013**, *560*, 82–88.
- (12) Yong, H.; Wang, S.; Ma, J.; Zhang, K.; Zhao, D.; Hu, J.; Zhang, Y. Dual-Tuning of de/Hydrogenation Kinetic Properties of Mg-Based Hydrogen Storage Alloy by Building a Ni-/Co-Multi-Platform Collaborative System. *Int. J. Hydrogen Energy* **2021**, *46*, 24202.
- (13) Wang, X.; Xiao, X.; Zheng, J.; Hang, Z.; Lin, W.; Yao, Z.; Zhang, M.; Chen, L. The Dehydrogenation Kinetics and Reversibility Improvements of Mg(BH₄)₂ Doped with Ti Nano-Particles under Mild Conditions. *Int. J. Hydrogen Energy* **2021**, *46*, 23737.
- (14) El-Eskandarany, M. S.; Shaban, E. Contamination Effects on Improving the Hydrogenation/Dehydrogenation Kinetics of Binary Magnesium Hydride/Titanium Carbide Systems Prepared by Reactive Ball Milling. *Materials (Basel)*. **2015**, *8* (10), 6880–6892.
- (15) Gross, K. J.; Majzoub, E. H.; Spangler, S. W. The Effects of Titanium Precursors on Hydriding Properties of Alanates. *In Journal of Alloys and Compounds* **2003**, *356–357*, 423–428.
- (16) Schneemann, A.; White, J. L.; Kang, S.; Jeong, S.; Wan, L. F.; Cho, E. S.; Heo, T. W.; Prendergast, D.; Urban, J. J.; Wood, B. C.; Allendorf, M. D.; Stavila, V. Nanostructured Metal Hydrides for Hydrogen Storage. *Chem. Rev.* **2018**, *118*, 10775–10839.
- (17) Filinchuk, Y.; Richter, B.; Jensen, T. R.; Dmitriev, V.; Chernyshov, D.; Hagemann, H. Porous and Dense Magnesium Borohydride Frameworks: Synthesis, Stability, and Reversible Absorption of Guest Species. *Angew. Chemie Int. Ed.* **2011**, *50* (47), 11162–11166.
- (18) Leick, N.; Strange, N. A.; Schneemann, A.; Stavila, V.; Gross, K.; Washon, N.; Settle, A.; Martinez, M. B.; Gennett, T.; Christensen, S. T. Al₂O₃ Atomic Layer Deposition on Nanostructured γ -Mg(BH₄)₂ for H₂ Storage. *ACS Appl. Energy Mater.* **2021**, *4* (2), 1150–1162.
- (19) Saldan, I. Decomposition and Formation of Magnesium Borohydride. *Int. J. Hydrogen Energy* **2016**, *41*, 11201–11224.
- (20) Strange, N. A.; Leick, N.; Shulda, S.; Schneemann, A.; Stavila, V.; Lipton, A. S.; Toney, M. F.; Gennett, T.; Christensen, S. T. Reactive Vapor-Phase Additives toward Destabilizing γ -Mg(BH₄)₂ for Improved Hydrogen Release. *ACS Appl. Energy Mater.* **2022**, *5* (2), 1690–1700.
- (21) Herley, P. J.; Jones, W. Transmission Electron Microscopy of Beam-Sensitive Metal Hydrides. *Zeitschrift für Phys. Chemie* **1986**, *147* (1–2), 147–159.
- (22) Li, J.; Xu, J.; Li, B.; He, L.; Lin, H.; Li, H. W.; Shao, H. Advanced SEM and TEM Techniques Applied in Mg-Based Hydrogen Storage Research. *Scanning* **2018**, *2018*, 1.
- (23) Zavorotynska, O.; Deledda, S.; Vitillo, J.; Saldan, I.; Guzik, M.; Baricco, M.; Walmsley, J.; Muller, J.; Hauback, B. Combined X-Ray and Raman Studies on the Effect of Cobalt Additives on the Decomposition of Magnesium Borohydride. *Energies* **2015**, *8* (9), 9173–9190.
- (24) Beattie, S. D.; Setthanan, U.; McGrady, G. S. Thermal Desorption of Hydrogen from Magnesium Hydride (MgH₂): An in Situ Microscopy Study by Environmental SEM and TEM. *Int. J. Hydrogen Energy* **2011**, *36* (10), 6014–6021.
- (25) Li, H.-W.; Miwa, K.; Ohba, N.; Fujita, T.; Sato, T.; Yan, Y.; Towata, S.; Chen, M. W.; Orimo, S. Formation of an Intermediate Compound with a B₁₂H₁₂ Cluster: Experimental and Theoretical Studies on Magnesium Borohydride Mg(BH₄)₂ Related Content First-Principles Study of a Double-Cation Alkali Metal Borohydride LiK(BH₄)₂. *Nanotechnology* **2009**, *20*, 204013.
- (26) Schneemann, A.; Wan, L. F.; Lipton, A. S.; Liu, Y. S.; Snider, J. L.; Baker, A. A.; Sugar, J. D.; Spataru, C. D.; Guo, J.; Autrey, T. S.; Jørgensen, et al. Nanoconfinement of Molecular Magnesium Borohydride Captured in a Bipyridine-Functionalized Metal-Organic Framework. *ACS Nano* **2020**, *14* (8), 10294–10304.
- (27) White, J. L.; Strange, N. A.; Sugar, J. D.; Snider, J. L.; Schneemann, A.; Lipton, A. S.; Toney, M. F.; Allendorf, M. D.; Stavila, V. Melting of Magnesium Borohydride under High Hydrogen Pressure: Thermodynamic Stability and Effects of Nanoconfinement. *Chem. Mater.* **2020**, *32* (13), 5604–5615.
- (28) Soloveichik, G. L.; Gao, Y.; Rijssenbeek, J.; Andrus, M.; Kniajanski, S.; Bowman, R. C.; Hwang, S.-J.; Zhao, J.-C. Magnesium Borohydride as a Hydrogen Storage Material: Properties and Dehydrogenation Pathway of Unsolvated Mg(BH₄)₂. *Int. J. Hydrogen Energy* **2009**, *34* (2), 916–928.
- (29) Berlin, J. Analysis of Boron with Energy Dispersive X-Ray Spectrometry: Advances in Light Element Analysis with SDD Technology; *Imaging & Microscopy* **2011**; Vol. 13.
- (30) Schindelin, J.; Arganda-Carreras, I.; Frise, E.; Kaynig, V.; Longair, M.; Pietzsch, T.; Preibisch, S.; Rueden, C.; Saalfeld, S.; Schmid, B.; Tinevez, J. Y. Fiji: An Open-Source Platform for Biological-Image Analysis. *Nat. Methods* **2012**, *9*, 676–682.
- (31) Dimitrievska, M.; White, J. L.; Zhou, W.; Stavila, V.; Klebanoff, L. E.; Udovic, T. J. Structure-Dependent Vibrational Dynamics of Mg(BH₄)₂ Polymorphs Probed with Neutron Vibrational Spectroscopy and First-Principles Calculations. *Phys. Chem. Chem. Phys.* **2016**, *18* (36), 25546–25552.
- (32) Severa, G.; Rönnebro, E.; Jensen, C. M. Direct Hydrogenation of Magnesium Boride to Magnesium Borohydride: Demonstration of > 11 Weight Percent Reversible Hydrogen Storage. *Chem. Commun.* **2010**, *46* (3), 421–423.
- (33) Paterson, W. G.; Onyszczuk, M. the Interaction of Hydrazine with Boron and Aluminum Halides. *Can. J. Chem.* **1963**, *41* (8), 1872–1876.
- (34) Hügler, T.; Kühnel, M. F.; Lentz, D. Hydrazine Borane: A Promising Hydrogen Storage Material. *J. Am. Chem. Soc.* **2009**, *131* (21), 7444–7446.
- (35) Goubeau, J.; Ricker, E. Borinhydrazin Und Seine Pyrolyseprodukte. *ZAAC - J. Inorg. Gen. Chem.* **1961**, *310* (3), 123–142.
- (36) Hoekstra, H. R.; Katz, J. J. The Preparation and Properties of the Group IV-B Metal Borohydrides. *J. Am. Chem. Soc.* **1949**, *71* (7), 2488–2492.
- (37) Dain, C. J.; Downs, A. J.; Goode, M. J.; Evans, D. G.; Nicholls, K. T.; Rankin, D. W. H.; Robertson, H. E. Molecular Structure of Gaseous Titanium Tris(Tetrahydroborate), Ti(BH₄)₃: Experimental Determination by Electron Diffraction and Molecular Orbital Analysis of Some Ti(BH₄)₃ Derivatives. *J. Chem. Soc. Dalton Trans.* **1991**, *4*, 967–977.
- (38) Hino, S.; Fonnelløp, J. E.; Corno, M.; Zavorotynska, O.; Damin, A.; Richter, B.; Baricco, M.; Jensen, T. R.; Sørby, M. H.; Hauback, B. C.

Halide Substitution in Magnesium Borohydride. *J. Phys. Chem. C* **2012**, *116* (23), 12482–12488.

(39) Ye, F.; Xu, M.; Dai, S.; Tieu, P.; Ren, X.; Pan, X. In Situ TEM Studies of Catalysts Using Windowed Gas Cells. *Catalysts* **2020**, *10* (7), 779.

(40) Zanella, P.; Crociani, L.; Masciocchi, N.; Giunchi, G. Facile High-Yield Synthesis of Pure, Crystalline Mg(BH₄)₂. *Inorg. Chem.* **2007**, *46* (22), 9039–9041.

(41) Hurst, K. E.; Heben, M. J.; Blackburn, J. L.; Gennett, T.; Dillon, A. C.; Parilla, P. A. A Dynamic Calibration Technique for Temperature Programmed Desorption Spectroscopy. *Rev. Sci. Instrum.* **2013**, *84*, 025103.

(42) Hoffman, A. S.; Singh, J. A.; Bent, S. F.; Bare, S. R. In Situ Observation of Phase Changes of a Silica-Supported Cobalt Catalyst for the Fischer–Tropsch Process by the Development of a Synchrotron-Compatible in Situ/Operando Powder X-Ray Diffraction Cell. *J. Synchrotron Radiat.* **2018**, *25* (6), 1673–1682.

Recommended by ACS

Chemically Assisted Precompression of Hydrogen Molecules in Alkaline-Earth Tetrahydrides

Miriam Peña-Alvarez, Ross T. Howie, *et al.*

SEPTEMBER 02, 2022

THE JOURNAL OF PHYSICAL CHEMISTRY LETTERS

READ 

External Electric Field-Induced Phase Transition of a Series of Energetic Pentazole Crystals: A First-Principles Study

Xiaowei Wu, Jian-Guo Zhang, *et al.*

JULY 01, 2022

CRYSTAL GROWTH & DESIGN

READ 

Structural Stability and Phase Transitions in Zeolite A: An In Situ High Pressure–High Temperature Investigation

K. A. Irshad, Hrudananda Jena, *et al.*

AUGUST 24, 2022

INORGANIC CHEMISTRY

READ 

Series of Fluorinated Benzimidazole-Substituted Nitronyl Nitroxides: Synthesis, Structure, Acidity, Redox Properties, and Magnetostructural Correlations

Evgeny Tretyakov, Dominique Luneau, *et al.*

OCTOBER 05, 2022

THE JOURNAL OF ORGANIC CHEMISTRY

READ 

Get More Suggestions >